



HAL
open science

Structural and electronic analysis of bimetallic thiolate complexes of group-5 transition metal ions

U. Kaur, K. Saha, S. Bairagi, A. Das, T. Roisnel, T.K. Paine, S. Ghosh

► **To cite this version:**

U. Kaur, K. Saha, S. Bairagi, A. Das, T. Roisnel, et al.. Structural and electronic analysis of bimetallic thiolate complexes of group-5 transition metal ions. *Journal of Organometallic Chemistry*, 2021, 949, pp.121943. 10.1016/j.jorganchem.2021.121943 . hal-03335245

HAL Id: hal-03335245

<https://hal.science/hal-03335245>

Submitted on 7 Sep 2021

HAL is a multi-disciplinary open access archive for the deposit and dissemination of scientific research documents, whether they are published or not. The documents may come from teaching and research institutions in France or abroad, or from public or private research centers.

L'archive ouverte pluridisciplinaire **HAL**, est destinée au dépôt et à la diffusion de documents scientifiques de niveau recherche, publiés ou non, émanant des établissements d'enseignement et de recherche français ou étrangers, des laboratoires publics ou privés.

Highlights:

- A series of binuclear thiolate complexes of group-5 metals have been synthesised and the role of metal and associated thiolate ligands influencing the structural and electronic properties of these complexes has been described.
- The experimental results have been complemented and rationalized through DFT studies.

Journal Pre-proof

Structural and electronic analysis of bimetallic thiolate complexes of group-5 transition metal ions

Urminder Kaur,^a Koushik Saha,^a Subhash Bairagi,^a Abhishek Das,^b Thierry Roisnel,^c Tapan Kanti Paine,^{*b} and Sundargopal Ghosh^{*a}

^a Department of Chemistry, Indian Institute of Technology Madras, Chennai 600 036, India

^b School of Chemical Sciences, Indian Association for the Cultivation of Science, 2A and 2B Raja S.C. Mullick Road, Jadavpur, Kolkata 700032, India

^c Univ Rennes, CNRS, Institut des Sciences Chimiques de Rennes, UMR 6226, F-35042 Rennes, France

Email : sghosh@iitm.ac.in (S. Ghosh), ictkp@iacs.res.in (T. Paine)

Dedicated to Professor Pradeep Mathur on the occasion of his 65th birthday in recognition of his outstanding contributions to the area of organometallic chemistry.

Abstract:

The chemistry of group-5 transition metals, namely vanadium, niobium, and tantalum supported by thiolate ligand framework, has been described. Special emphasis has been given to the electronic and structural properties of binuclear thiolate complexes of group-5 metals exhibiting interesting coordination modes of the chelating thiolate ligands. The mild thermolysis of $[(\text{CH}_2\text{S}_2)_4\text{B}]\text{Na}_5$ with $[\text{Cp}^*\text{VCl}_2]_3$ afforded the divanadium trithiocarbonate complex, $[(\text{Cp}^*\text{V})_2(\mu\text{-CS}_3\text{-}\kappa^2\text{S,S}')(\mu\text{-H}_2\text{CS}_2\text{-}\kappa^2\text{S}'',\text{S}''')] \text{ (1)}$ along with $[\{\text{S}(\text{CH}_2\text{S})_2\}\text{VOCp}^*] \text{ (2)}$. The single crystal X-ray structure of **1** illustrates that the trithiocarbonate and methanedithiolate ligands are symmetrically coordinated to two $\{\text{Cp}^*\text{V}\}$ units. However, the reaction of the heavier group-5 metal precursor, $[\text{Cp}^*\text{NbCl}_4]$ with $[(\text{CH}_2\text{S}_2)_4\text{B}]\text{Na}_5$ at 60 °C in toluene produced a bimetallic trithiolate complex $[(\text{Cp}^*\text{Nb})_2(\mu\text{-SCS}_2\text{-}\kappa^1\text{S}:\kappa^3\text{C,S',S}'')(\mu\text{-S})_2] \text{ (3)}$ along with $[(\text{Cp}^*\text{Nb})_2(\mu,\eta^2:\eta^2\text{-SH}_3\text{B})(\mu\text{-S})(\mu\text{-H}_2\text{CS}_2\text{-}\kappa^2\text{S,S}')]$. In a similar manner, $[\text{Cp}^*\text{TaCl}_4]$ led to the formation of ditantalum thiolate complexes $[(\text{Cp}^*\text{Ta})_2(\mu\text{-S})(\mu\text{-S}_2\text{CH}_2\text{CHS}_2\text{-}\kappa^2\text{S}:\kappa^2\text{S}',\text{S}'')(\mu\text{-H})(\mu\text{-S}_2\text{CH}_2\text{-}$

κ^2S''',S''''] (**4**) and $[Cl(Cp^*Ta)_2(\mu-H)(\mu-S_2CH_2-\kappa^2S,S')(\mu-S)(\mu-S_2CH_2-\kappa^2S'';\kappa^1S''')]$ (**5**) along with $[(Cp^*Ta)_2(\mu-S)\{\mu-(BH_2S)(CH_2S)_2(BS_3)-\kappa^2B;\kappa^2S;\kappa^4S',S'',S''',S''''\}]$. However, the reaction of $LiBH_4 \cdot THF$ with $[Cp^*TaCl_4]$ followed by the thermolysis in presence of $S_2C \cdot PPh_3$ led to the formation of $[(Cp^*Ta)_2(\mu-S)(\mu-S_2CH_2-\kappa^2S,S')(\mu-H)(\mu-CHS_3-\kappa^2S'';\kappa^2S''',S'''')]$ (**6**) along with $[(Cp^*Ta)_2(\mu-S_2CH_2-\kappa^2S,S')_2(\mu-H)(\mu,\eta^2:\eta^2-B_2H_5)]$ (**I**) and $[(Cp^*Ta)_2(\mu,\eta^2:\eta^2-B_2H_6)_2]$ (**II**). Complex **3** is an example of trithiolate $\{CS_3\}$ stabilized bimetallic niobium complex. The (dimercaptomethyl)-methanedithiolate ligand ($C_2H_3S_4$) in **4** is coordinated to both the tantalum centres via three sulfur donors and displayed exclusive bonding mode $(\mu,\kappa^2S;\kappa^2S',S'')$. Complex **5** consists of two methanedithiolate ligands (S_2CH_2) with different coordination towards the metal centres, whereas methanetrithiolate (HCS_3) and methanedithiolate (S_2CH_2) units are symmetrically coordinated to both the tantalum centres in complex **6**. This study demonstrates that the electronic properties of these complexes vary depending on the metal centres and thiolate ligands. This is reflected in the paramagnetic behaviour of the vanadium complex **1**. In contrast, the niobium and tantalum thiolate complexes **3**, **4**, **5** and **6** are diamagnetic. Further, theoretical investigations provided the insights into the electronic structures and bonding of these group-5 metal thiolate complexes.

Keywords: Thiolate, Tantalum, Niobium, Vanadium, Paramagnetic

1. Introduction

The chemistry of early transition metal complexes incorporating thiolate ligands has received considerable attention over the years for several reasons. The close relevance of these transition metal thiolates to certain biological systems and industrial catalysts,^{1,2} their potentiality in the chemistry related to S–C bond cleavage and desulfurization,³ their efficacy in the synthesis of metal sulfide as well as organosulfur materials by MOCVD processes,^{4a} are some of the

motivating facts which led to the development of their chemistry. The increasing interest in these complexes stems from their resemblance with the metalloproteins such as metallothioneins or nitrogenase.² Moreover, the long-known polymetallic thiolate clusters act as synthetic models for biologically active sites, whereas polyoxometalates have shown promising biological and biochemical effects recently with their antiviral, antitumoral, and antibiotic properties.^{4b}

Although the diamagnetic transition metal thiolates are an enormously rich class of compounds, the chemistry of paramagnetic metal thiolates appears to be relatively less explored and thus becomes an exciting and active research field. The isolation of first homoleptic paramagnetic group-5 thiolate complex $[V_2(SCH_2CH_2S)_4]$ in 1983 spurred the chemistry of transition metal thiolates exhibiting paramagnetic behaviour and became the focus for many inorganic and organometallic chemists.⁵ The detailed investigation on magnetic as well as the structural properties of these paramagnetic complexes is important for understanding the nature of exchange interactions between the paramagnetic metal ions. In particular, the contribution from direct exchange through M–M bonds and from super exchange via bridged ligands can be estimated. Therefore, a thorough investigation in this matter becomes of interest.

Our recent studies are focused on the syntheses of transition metal complexes containing metal centres bridged by thiolate/dithiolate ligands.⁶⁻⁹ In our previous report, we have isolated and structurally characterised a classical $[B_2H_5]^-$ ion, $[(Cp^*Ta)_2(\mu-S_2CH_2-\kappa^2S:\kappa^2S')_2(\mu-H)(\mu,\eta^2:\eta^2-B_2H_5)]$, **I**.⁹ Later, we developed a new methodology to synthesize different thiolate complexes of group-5 metals that exhibit novel coordination modes of sulfur-containing ligands with interesting electronic properties.⁸ For example, the room temperature reaction of $[(CH_2S_2)_4B]Na_5$ ¹⁰ with $[Cp^*VCl_2]_3$ generated diamagnetic as well as paramagnetic thiolate complexes. In contrast, niobium and tantalum yielded only diamagnetic species. Thus, we were

interested to know the role of transition metal ions as well as thiolate ligand that determined the nature of the thiolate complexes. Thus, we have revisited this system with different reaction conditions. This report provides a detailed account of the chemistry of group-5 metal precursors with $[(\text{CH}_2\text{S}_2)_4\text{B}]\text{Na}_5$. In addition, the density functional theoretical calculations were carried out to provide a clear picture of the bonding, electronic structures and transitions of these thiolate complexes.

2. Results and discussion

2.1 Reactivity of $[(\text{CH}_2\text{S}_2)_4\text{B}]\text{Na}_5$ with $[\text{Cp}^*\text{VCl}_2]_3$

The reaction of $[(\text{CH}_2\text{S}_2)_4\text{B}]\text{Na}_5$ with $[\text{Cp}^*\text{VCl}_2]_3$ at 60 °C over 6 h allowed the formation of $[(\text{Cp}^*\text{V})_2(\mu\text{-CS}_3\text{-}\kappa^2\text{S,S}')(\mu\text{-H}_2\text{CS}_2\text{-}\kappa^2\text{S'',S'''})]$, **1**, and $[\{\text{S}(\text{CH}_2\text{S})_2\}\text{OVCP}^*]^8$, **2**, in 11 and 32% yield, respectively (Scheme 1). The structural characterisation of **1** was carried out by single crystal X-ray diffraction study and its identity is described below.

(Scheme 1 near here)

To our surprise, the ^1H NMR spectrum of **1** did not show any meaningful chemical shifts in the diamagnetic region. The mass spectrometric data of **1** displayed an ion peak at $m/z = 559.0039$ $[\text{M}+\text{H}]^+$ with the isotope distribution pattern corresponding to the molecular formula $\text{C}_{22}\text{H}_{32}\text{S}_5\text{V}_2$ (Fig. S3). This spectrometric data was not sufficient to propose the structure of **1**. The slow evaporation of CH_2Cl_2 /hexane (30:70) solution of **1** at 5 °C produced the single crystals appropriate for X-ray diffraction.

As shown in Fig. 1, the solid-state X-ray structure of **1** displays that the methanedithiolate (CH_2S_2) and trithiocarbonate (CS_3) ligands symmetrically coordinated to two $\{\text{Cp}^*\text{V}\}$ units in $\{\mu,\kappa^2\}$ fashion. The mirror plane is passing through the molecule which contains both

methanedithiolate and trithiocarbonate ligands. Both the metal centres in **1** adopted a pseudo-octahedral coordination geometry. The trithiocarbonate ligand in **1** shows two types of C–S bond distances, 1.747(4) (C21–S1) and 1.622(4) Å (C21–S3), corresponding to single and double bond distances, respectively.¹² The V–V single bond length of 2.5548(7) Å is shorter as compared to those of reported bimetallic vanadaborane complexes, such as [(CpV)₂(μ,η²:η²-B₂H₆)₂]¹¹ (2.787(2) Å) and [(Cp*V)₂(μ,η²:η²-BH₃S)(μ-SPh)₂],^{12a} (2.6816(12) Å). The C22–S4 (1.835(4) Å) and C22–S5 (1.833(4) Å) bond distances are in the single bond range and similar to tungsten methanedithiolate complex, [(Cp*W)₂(μ-S₂CH₂-κ²S,S')(μ-S)₂]¹³ (c.a. 1.85 Å). In addition, the Cp* ligands are in eclipsed positions with respect to the V1–V2 bond. The V–S–V angles in the range of 62.77–63.61° are comparable to other bimetallic vanadium thiolate complexes.¹³ The importance of complex **1** can be correlated to [(CpMo)₂(μ-S₂CH₂-κ²S,S')(μ-S)₂], which participated in the hydrogenation of olefins.¹⁴ Therefore, **1** is a unique entry to the family of bimetallic thiolate complexes.

(Fig. 1 near here)

Density functional theory (DFT) calculations at the BP86/def2-TZVP level were performed to understand the electronic and bonding situation in **1**. The optimized geometry of **1** matches well with the solid-state structure. An energy gap of 0.85 eV between its HOMO and LUMO is observed in the molecular orbital (MO) analysis of **1** and that is consistent with its thermodynamic stability. Based on MO analysis, the α-SOMO-2 of **1**, discloses the overlap of the *d_z²* orbitals of both the vanadium centres indicating a strong bonding interaction between the two vanadium centres (Fig. 2a). This is further confirmed by the Wiberg bond index (WBI) of V–V bond (0.91) and the contour line diagram of **1** (Fig. 2d). As shown in Fig. 2b, the α-SOMO-9 of **1** shows the localization of electron density on all the sulfur atoms except S3 atom, in which

the electron density is delocalized over S3 and C21 atoms by the side-to-side overlap of the atomic orbitals i.e., π -bonding and confirms the presence of C=S double bond. The α -SOMO-13 of **1** shows the d - p orbital interaction between vanadium and sulfur. Furthermore, the Laplacian electron density plot of **1** shows the bonding scenario of the plane consisting CS₃ and CH₂S₂ ligands, which is perpendicular to the V–V bond (Fig. 2e). A negative natural charge on carbon and a positive natural charge on sulfur atoms of the methanedithiolate and trithiocarbonate ligands are observed by performing the natural bond orbital (NBO) analysis of **1** (Table S1).

(Fig. 2 near here)

Vanadium is found in several oxidation states that vary from (-1) to (+5), and among them vanadium ions in +2, +3 and +4 oxidation states are paramagnetic.¹⁵ Vanadium(III) is generally found in marine invertebrates, cofactor of nitrogenase, nitrogen-fixing bacteria and other species. Recent investigation suggested that vanadium(III) thiolate complexes are stable in physiological conditions.¹⁶ Therefore, the electronic properties of vanadium thiolate complexes are of interest.

To get information in this regard, complex **1** was subjected to EPR spectroscopy. Vanadium(III) complexes are generally EPR silent in conventional conditions due to their large zero-field splitting and integer spin number ($S = 1$). For such systems, high-frequency or high-field electron paramagnetic resonance (HF-EPR) techniques are required to understand the magnetic properties of vanadium(III) species.¹⁷ However, conventional X-band EPR spectroscopy is often useful in understanding the electronic structure of half-integer spin vanadium (II) ($S = 3/2$) or vanadium (IV) ($S = 1/2$) complexes. Interestingly, the X-band EPR spectrum of the solid sample of **1** at 77 K displays the eight-line pattern for vanadium (^{51}V ; $I = 7/2$) with anisotropic g and A values (Fig. 3). In addition, each vanadium hyperfine exhibits eight-line superhyperfine splitting. These unique splitting patterns in the EPR spectrum do not arise

from a monomeric complex, rather two vanadium centres are connected to each other. In this case, the nuclear spins of one vanadium centre interact with the electron spin on the other vanadium centre. Thus, the spectral data confirms the existence of a strong bonding interaction between the two vanadium centres, as observed in the single crystal X-ray diffraction data and DFT calculations.

(Fig. 3 near here)

The experimental spectrum was simulated taking the above-mentioned electronic scenario into consideration. Simulation of the experimental spectrum yields the parameters $g_x = 1.990$, $g_y = 1.995$, $g_z = 1.95$, and the hyperfine coupling constants $A_x = 50 \times 10^{-4} \text{ cm}^{-1}$, $A_y = 60 \times 10^{-4} \text{ cm}^{-1}$, and $A_z = 113 \times 10^{-4} \text{ cm}^{-1}$. The super-hyperfine coupling constants are calculated to be $A_x = 13.3 \times 10^{-4} \text{ cm}^{-1}$, $A_y = 20 \times 10^{-4} \text{ cm}^{-1}$, and $A_z = 10 \times 10^{-4} \text{ cm}^{-1}$. The EPR parameters with all g values < 2 and large A_z value indicate that the unpaired electron resides in the d_{xy} orbital of vanadium. The energy gap between the d_{xy} and $d_{x^2-y^2}$ orbitals is larger compared to that between d_{xz}/d_{yz} and d_{xy} orbitals of vanadium. An increased covalency in the equatorial plane likely responsible for low g_z value in the complex. As shown in Fig. 4, the molecular orbitals housing the two unpaired electrons indicate non-orthogonality of the d orbitals of vanadium in the α and β subspaces. Therefore, it is expected that the electrons on two vanadium centres would interact with each other. While the electrons in the d_{z^2} orbitals are involved in V–V bonding, the d_{xy} orbitals of vanadium do not overlap appreciably due to the small V–S–V angle (*vide supra*). As a result, the electron in the d_{xy} orbital of each vanadium centre of the weakly interacting symmetric dimer gives rise to the EPR signals.

(Fig. 4 near here)

2.2 Reactivity of $[(CH_2S_2)_4B]Na_5$ with $[Cp^*MCl_4]$ ($M = Nb$ and Ta)

Mild thermolysis of $[Cp^*NbCl_4]$ with $[(CH_2S_2)_4B]Na_5$ in toluene yielded $[(Cp^*Nb)_2(\mu-SCS_2-\kappa^1S:\kappa^3C,S',S'')(\mu-S)_2]$, **3** and $[(Cp^*Nb)_2-(\mu,\eta^2:\eta^2-SH_3B)(\mu-S)(\mu-H_2CS_2-\kappa^2S,S')]^8$ (Scheme 2). Whereas In case of tantalum, the reaction of $[(CH_2S_2)_4B]Na_5$ with $[Cp^*TaCl_4]$ at room temperature yielded $[(Cp^*Ta)_2(\mu-S)(\mu-S_2CH_2CHS_2-\kappa^2S:\kappa^2S',S'')(\mu-H)(\mu-S_2CH_2-\kappa^2S''',S'''')]$, **4**, and $[Cl(Cp^*Ta)_2(\mu-H)(\mu-S_2CH_2-\kappa^2S,S')(\mu-S)(\mu-S_2CH_2-\kappa^2S''':\kappa^1S''')]$, **5**, in 28 and 15% yields, respectively (Scheme 2). The reaction also yielded $[(Cp^*Ta)_2(\mu-S)\{\mu-(BH_2S)(CH_2S)_2(BS_3)-\kappa^2B:\kappa^2S:\kappa^4S',S'',S''',S''''\}]^8$. The spectroscopic and structural characterisations of complexes **3-5** are discussed below in detail.

(Scheme 2 near here)

Complex **3** was isolated as a green solid with 16% yield. The 1H NMR spectrum of **3** shows resonance at $\delta = 2.17$ ppm corresponding to the methyl protons of Cp^* units which is further supported by the $^{13}C\{^1H\}$ NMR spectrum (Figs S4 and S5). The $^{11}B\{^1H\}$ NMR spectrum showed no resonance indicating the absence of boron. The mass spectrometric analysis showed a molecular ion peak at m/z 628.9130 consistent with the molecular formula of $C_{21}H_{31}Nb_2S_5$ ($[M+H]^+$) (Fig. S6). The green crystals of **3** were obtained by slow evaporation of the CH_2Cl_2 /hexane (30:70) solution of the complex at 5 °C.

The single crystal X-ray diffraction studies revealed the identity of **3** as $[(Cp^*Nb)_2(\mu-SCS_2-\kappa^1S:\kappa^3C,S',S'')(\mu-S)_2]$ (Fig. 5). Note that, here we have discussed the data of one amongst the two independent molecules present in the asymmetric unit of **3**. The structure of **3** clearly displays that a trithiolate (S_3C) ligand is coordinated to two $\{Cp^*Nb\}$ units through one carbon and three sulfur atoms in a unique binding mode which can be described as $\{\mu,\kappa^1S:\kappa^3C,S',S''\}$. The mirror plane is passing through the molecule, which contains both the Nb atoms along with C31 and S5

atoms of {CS₃} unit. The {CS₃} moiety of trithiolate ligand is nearly planar with the sum of S-C-S bond angles of 359.64° (S1-C31-S2 112.26(14)°, S1-C31-S5 123.46(16)° and S2-C31-S5 123.92(15)°). The Nb–Nb bond length of 2.9705(3) Å is in accord with that of other binuclear niobium complexes, for example, [(Cp*Nb)₂(CH₂SiMe₃)₂(μ-S)₂] (2.978 Å) and [(Cp*Nb)₂(C₃H₅)₂(μ-S)₂] (3.141 Å).¹⁸ The C–S bond distances (C31-S1 1.756(3) Å, C31-S2 1.746(3) Å, C31-S5 1.776(3) Å) of trithiolate ligand in **3** are fall within single C–S bond distance observed in various metal thiolate complexes.^{12b-c, 19}

(Fig. 5 near here)

In addition, the average Nb–S distance for Nb2 is 2.323 Å, which is relatively smaller compared to that for Nb1 (2.4865 Å). This may be due to the unsymmetrical bonding of the trithiolate ligand towards the metal centres in **3**. The Nb–S–Nb angles Nb1-S3-Nb2 (75.81(2)°) and Nb1-S4-Nb2 (76.36(2)°) are comparable with the sulfur bridged niobium complex [(Cp*Nb)₂(CH₂Si-Me₃)₂(μ-S)₂]¹⁸ 78.8(1)°. One of the interesting aspects of complex **3** is the unique binding mode adopted by {CS₃} moiety of trithiolate ligand which differs significantly from those found in the previously reported complexes such as [(OC)₅(Cp*Mo)₂(μ-η²:η¹-CS₃)]^{13c}, and [{(η⁵-C₅H₃)₂(SiMe₂)(CMe₂)Mo(CO)₂]₂(μ-η¹:η²-CS₃)]²⁰ and complex **1** (Table 1).²¹ The different types of coordination modes known for the {CS₃} ligand in bimetallic systems are listed in Table 1. The bonding mode of trithiolate ligand present in **3** belongs to the type D where one carbon and two sulfur atoms are directly bonded to one metal centre while the third sulfur atom is attached to the other metal centre. Whereas, complex **1** resembles to the type C where the trithiocarbonate ligand binds with two metals through two sulfur donors in {κ²-S,S'} fashion.

(Table 1 near here)

The MO analysis of **3** disclosed that the HOMO-LUMO gap of **3** (1.32 eV) is greater than that of **1**. The Nb–Nb bonding interaction is depicted in HOMO-1 of **3**, where the *d* orbitals of both the Nb centres are delocalized to form the Nb–Nb bond (Fig. 6a). This Nb–Nb bonding is also verified by WBI of 0.45. The HOMO-8 of **3** reveals the bonding interaction (*d-p*) of Nb1-C31 and anti-bonding interaction of Nb2-C31 (Fig. 6b). The considerable WBI for the Nb1-C31 bond (0.535) indicated a meaningful bonding interaction between Nb1 and C31, which is also supported by the contour line diagram along Nb2-C31-Nb1 plane (Fig. 6d). The HOMO-25 of **3** showed the end-to-end *p-p* orbital overlap between C and S that indicated the presence of σ -(C-S) bonds of CS₃ moiety (Fig. 6c). In addition, the computed C–S bond lengths (C31-S1, C31-S2 and C31-S5) of 1.757, 1.762 and 1.787 Å are comparable to those observed in **3**. The Laplacian electron density plot along the S1-S2-S5 plane displayed a high amount of charge concentrations and the BCPs between C31-S1, C31-S2 and C31-S5 bonds specified strong bonding interactions (Fig. 6e).

(Fig. 6 near here)

Complexes **4** and **5** were characterised by multinuclear spectroscopy, mass spectrometry as well as single crystal X-ray diffraction analysis. The ¹¹B{¹H} NMR spectra of both **4** and **5** showed no resonances which suggested the formation of non-boron species. The ¹H chemical shifts at $\delta = 2.32, 2.26$ ppm (for **4**) and 2.31, 2.24 ppm (for **5**) were observed and that correspond to the methyl protons of two chemically and magnetically inequivalent Cp* ligands (Figs S9 and S12). The presence of Cp* units in complexes **4** and **5** is further corroborated by their respective ¹³C{¹H} NMR spectrum (Figs S8 and S11). Along with the Cp* ligands, the ¹H chemical shifts in the range of $\delta = 7.47-2.90$ ppm (for **4**) and $\delta = 7.43-4.15$ ppm (for **5**); and the ¹³C{¹H} chemical shifts at $\delta = 55.7-47.8$ ppm (for **4**) and $\delta = 56.7-43.3$ ppm (for **5**) confirmed the

presence of methylene units. The molecular ion peak at m/z 898.9876 ($[M+H]^+$) and 821.0310 ($[M-Cl]^+$) were observed corresponding to the molecular formula of $C_{23}H_{37}Ta_2S_7$ (for **4**) and $C_{22}H_{35}Ta_2S_5$ (for **5**), respectively (Figs S10 and S13). Storage of concentrated hexane/ CH_2Cl_2 (40:60) solutions at 5°C allowed the isolation of diffraction quality purple and orange crystals of **4** and **5**, respectively.

The solid-state X-ray structure of **4**, shown in Fig. 7 (left), consists of two (Cp^*Ta) units which are bridged by a sulfur, a methanedithiolate (S_2CH_2) and a (dimercaptomethyl)methanedithiolate ($S_4C_2H_3$) unit. The methanedithiolate ligand is bridged via two sulfur atoms in $\{\mu, \kappa^2 S''', S''''\}$ fashion, whereas the other $C_2H_3S_4$ moiety is bridged in $\{\mu, \kappa^2 S': \kappa^2 S'', S'''\}$ fashion. Notably, the coordination of (dimercaptomethyl)methanedithiolate unit towards the tantalum centres is exclusive as it coordinates to both the tantalum centres with three sulfur atoms. The unsymmetrical Ta–S bond distances (2.5641(14) vs 2.4470(13) Å) clearly indicate that the bridged sulfur atom is more loosely bonded with metal centres as compared to the terminal ones of the $C_2H_3S_4$ ligand. The bridged sulfur atom (S6) of this ligand forms an acute bridge ($\angle Ta1-S6-Ta2 = 73.49(4)^\circ$) with metal centres. The geometry around the sp^3 hybridized carbon atoms (C22 and C23) of this ligand are slightly deviated from the regular tetrahedron ($\angle S4-C22-S5 = 120.2(3)^\circ$ and $\angle S6-C23-S7 = 118.7(3)^\circ$). The average C–S bond distance (1.820 Å) of the $C_2H_3S_4$ unit is in the range of single bond length. The decrease in the Ta–Ta bond distance in **4** (3.1156(3) Å), as compared to that of $[(Cp^*Ta)_2(\mu-S_2CH-\kappa^2 C: \kappa^2 S, S')(\mu-S)(\mu-CHS_3-\kappa^2 S'': \kappa^2 S''', S'''')]$ (3.171 Å)⁸, is the resultant of decrease in the corresponding Ta–S–Ta angle. On the other hand, the sp^3 hybridized carbon atom of methanedithiolate ligand lies in a distorted tetrahedral configuration ($\angle S1-C21-S2 = 115.9(3)^\circ$).

(Fig. 7 near here)

In contrast, the solid-state X-ray structure of **5** consists of two {Cp*Ta} units which are bridged by methanedithiolate (S₂CH₂) ligands in two different coordination modes (Fig. 7 (right)). One of the methanedithiolate moiety bridged two Ta centres through two sulfur atoms in { $\mu, \kappa^2 S, S'$ } fashion, whereas the other one is bridged in { $\mu, \kappa^2 S'' : \kappa^1 S'''$ } fashion. Interestingly, this difference in the coordination of methanedithiolate units towards the tantalum centres is unique. Note that, the structure of **5** is disordered over two components with a site occupancy ratio of 0.64:0.36 (Fig. S1). The bridged sulfur atom (S4) of the S₂CH₂ ligand in **5** also makes an acute bridge ($\angle \text{Ta1-S4-Ta2} = 75.00(5)^\circ$) with the metals as observed in **4**. This increase in Ta-S-Ta angle results in a longer Ta-Ta bond distance in **5** (3.1483(8) Å). All the four C-S bond lengths in methane-dithiolate ligands (C21-S1 = 1.85(2) Å, C21-S2 = 1.77(2) Å, C22-S4 = 1.90(2) Å and C22-S5 = 1.81(3) Å) are in range of a typical C-S single bond distance.²¹ In addition to the two methanedithiolate ligands, a chlorine atom is directly bonded to one of the tantalum centres with a Ta1-Cl1 bond distance of 2.463(14) Å which is similar to that observed in complexes [(Cp*TaCl)₂(B₅H₁₁)] (2.465 Å), [Ta₂(PMe₃)₄(Cl)₄(H)₂] (2.418 Å), and [(Cp*TaCl)₂(B₅H₁₀Cl)] (2.441 Å).²²

The computational analyses of **4** and **5** revealed that the structural parameters of their optimized geometries are in good agreement with the experimentally observed values. The MO analyses revealed a larger HOMO-LUMO gap for **5** (1.91 eV) than that of **4** (1.70 eV). The HOMO-11 of **4** shows the Ta1-H36-Ta2 interaction (Fig. S16a) which is also confirmed by the Contour-line diagram of the Laplacian of the electron density along the Ta1-H36-Ta2 plane (Fig. S16b). The HOMO-18 of **5** shows end-to-end Cl1-Ta2 ($p_z-d_{z^2}$) overlap of atomic orbitals (or the presence of Cl1-Ta2 covalent bond) (Fig. S17a) which is also supported by the contour line diagram along the Ta1-Ta2-Cl1 plane (Fig. S17b).

2.3 Synthesis of tantalum thiolate complex, **6**

Isolation of classical $[\text{B}_2\text{H}_5]^-$ ion, **I** was achieved from the reaction of $\text{LiBH}_4 \cdot \text{THF}$ with $[\text{Cp}^*\text{TaCl}_4]$ in presence of $\text{S}_2\text{C} \cdot \text{PPh}_3$. Complex **I** was stabilized by binuclear tantalum template and methanedithiolate ligands.⁹ In order to isolate other diborane species, we reinvestigated this reaction under different reaction conditions. As a result, reaction of $\text{LiBH}_4 \cdot \text{THF}$ with $[\text{Cp}^*\text{TaCl}_4]$ followed by thermolysis in presence of $\text{S}_2\text{C} \cdot \text{PPh}_3$ was carried out. Although we did not able to isolate any diborane complexes, reaction yielded $[(\text{Cp}^*\text{Ta})_2(\mu\text{-S})(\mu\text{-S}_2\text{CH}_2\text{-}\kappa^2\text{S,S}')(\mu\text{-H})(\mu\text{-CHS}_3\text{-}\kappa^2\text{S}''\text{:}\kappa^2\text{S}'''\text{,S}''''\text{})]$, **6** along with **I** and $[(\text{Cp}^*\text{Ta})_2(\mu,\eta^2\text{:}\eta^2\text{-B}_2\text{H}_6)_2]$ ²², **II** (Scheme 3). The ^1H chemical shift at $\delta = 2.23$ ppm, corresponding to the Cp^* protons in **6**, are observed (Fig. S13) and further supported by the $^{13}\text{C}\{^1\text{H}\}$ NMR spectrum (Fig. S14). The absence of $^{11}\text{B}\{^1\text{H}\}$ signal for **6** suggested a non-boron species. The mass spectrum of **6** displayed a molecular ion peak at m/z 874.9845 $[\text{M}+\text{Na}]^+$ (Fig. S15). Several attempts to obtain good crystals of **6** for single crystal X-ray diffraction studies were unsuccessful. However, all the spectroscopic and mass spectrometric data along with the X-ray diffraction studies of a weakly diffracted crystal provided the core structure of **6** as $[(\text{Cp}^*\text{Ta})_2(\mu\text{-S})(\mu\text{-S}_2\text{CH}_2\text{-}\kappa^2\text{S,S}')(\mu\text{-H})(\mu\text{-CHS}_3\text{-}\kappa^2\text{S}''\text{:}\kappa^2\text{S}'''\text{,S}''''\text{})]$ (Fig. S2). Complex **6** consists of methanetrithiolate (HCS_3) and methanedithiolate (H_2CS_2) ligands symmetrically bridged between two $\{\text{Cp}^*\text{Ta}\}$ units in $\{\mu,\kappa^2\text{S,S}'\}$ and $\{\mu,\kappa^2\text{S}''\text{:}\kappa^2\text{S}'''\text{,S}''''\}$ fashion. It is interesting to note that complexes **4**, **5** and **6** are analogous to each other containing $\{\text{S}_4\text{C}_2\text{H}_3\}$, $\{\text{S}_2\text{CH}_2\}$ and $\{\text{S}_3\text{CH}\}$ ligands, respectively, in addition to the presence of a common methanedithiolate unit.

(Scheme 3 near here)

In order to understand the bonding situation in **4**, **5** and **6**, the computational studies were performed at the BP86/def2-TZVP level of theory. The MO analyses revealed that the HOMOs

of these complexes are localized over the S atoms (*p* orbital) whereas the LUMOs are mostly centred on both the tantalum atoms (*d*-orbital) along with a little contribution from the ligand. The WBI values of 0.32, 0.31 and 0.32 in **4**, **5** and **6**, respectively revealed a weak Ta–Ta bonding interaction. Further, the MO analysis showed that the HOMO-LUMO energy gap increases in the order **4** < **5** < **6** (Fig. 8). The NBO analyses revealed that the natural charge on both the Ta atoms is negative and quantitatively similar in **4** and **6**. Whereas, in the case of **5**, although the natural charge on Ta1 is negative as usual, it is positive on Ta2. This may be due to the direct Ta2-Cl bonding in which Cl atom acted as an electron withdrawing group. The natural charges on all the S atoms are positive due to charge transfer to metal centre except the bridging sulfur which is also reflected by the higher natural valence population as compared to other sulfur atoms.

(Fig. 8 near here)

Having a series of binuclear metal thiolate complexes in hand, we were interested to examine their structural parameters with other transition metal thiolate species, listed in Table 2.^{8,23} Amongst the listed complexes, it is observed that as the metal centre varies, there is a change in M–M, M–S bond lengths as well as the M–S–M bond angle. For example, on moving from V-complex **1** to Ta-complex **5**, there is an increase in the M–M and avg. M–S bond distances from 2.5548 Å to 3.1483 Å and 2.439 Å to 2.478 Å, respectively, which is further supported by calculated values (Table S1). The M–S–M bond angle also increases from 62.77° to 81.43°. This may be attributed to the **increase in the atomic radius** of the transition metal on moving from vanadium to tantalum, which results in the elongation of M–M and M–S bonds and causes the M–S–M bond angles to become less acute.²⁴ In addition, the ${}^2J_{\text{H-H}}$ coupling constant for the

methanedithiolate protons in the listed tantalum thiolate complexes were found to be in the range of 10-13 Hz.

(Table 2 near here)

2.4 UV-vis absorption studies of complexes **1**, **3**, **4**, **5** and **6**

The UV-vis absorption spectroscopy helped to measure the optical properties of complexes **1**, **3**, **4**, **5** and **6**. Their UV-Vis spectra reveal multiple bands around 280-600 nm (Fig. 9). The high-energy absorption bands around 280-290 nm are for the $\pi-\pi^*$ transition of Cp* ligands and that is characteristic of most of the Cp* based-metal complexes.²⁵ The low-energy bands around 340-550 nm are assigned to charge transfer bands.^{8,26}

(Fig. 9 near here)

To get information about the electronic transitions, time dependent DFT calculations were carried out. These calculations suggest that the possible numbers of transitions are more in complex **1** compared to those of **3**, **4**, **5** and **6** (Table S2-S6, Fig. S18-S22). This accounts for the paramagnetic behaviour observed in **1**, showing α and β subspaces, whereas complexes **3**, **4**, **5** and **6** are diamagnetic in nature. The molecular orbitals related to the most intense electronic transitions for **1**, **3**, **4**, **5** and **6** are shown in Fig. S23-S27. In complex **1**, the absorption near 341 nm may be assigned to the electronic transition corresponding to HOMO-1(α) \rightarrow LUMO(α), HOMO-1(α) \rightarrow LUMO+2(α), which may be considered as an intramolecular MLCT transition. The low intensity absorptions near 463 and 543 nm could be the intramolecular LMCT transitions corresponding to HOMO(α) \rightarrow LUMO(α) and HOMO(α) \rightarrow LUMO+5(α), respectively. The absorption band at 347 nm for complex **3** corresponds to MLCT transitions, whereas the absorptions near 458 and 533 nm seem to be intramolecular LMCT transitions. Similarly, the absorptions at \sim 370 nm for complexes **4**, **5** and **6** appear due to MLCT transitions, whereas

those in 432-511 nm region are mainly due to intramolecular LMCT transitions. A comparison among the low-intensity absorption bands ranged from 432-543 nm reveals a blue shift from V to Nb to Ta, which is also in accord with their HOMO-LUMO energy gaps. In contrast, a red shift is observed in case of high intensity absorption bands ranged from 341-371 nm.

3. Conclusions

In this report, we have demonstrated a series of binuclear thiolate complexes of group-5 metals

and the studies show that the metal as well as the associated ligands play important roles in tuning the structural and electronic properties of these complexes. The V–V bond in the binuclear vanadium complex **1** influences the electronic properties of the complex. Furthermore, the vanadium thiolate complex provides structural model systems, which might be useful for the identification and understanding of vanadium-sulfur centres in metallobiomolecules. In the latter context, we have discussed the niobium complex **3**, which shows a unique binding mode of trithiolate ligand. In addition to this, the tantalum complexes **4**, **5** and **6** display a variety of thiolate ligands, such as (dimercaptomethyl)methanedithiolate, methanedithiolate and methanetrithiolate, coordinated to the tantalum centres. These complexes show diamagnetic behaviour in contrast to the vanadium complex **1**.

4. Experimental details

4.1 General procedures and instrumentation

All the syntheses were performed under argon atmosphere using standard Schlenk line and glove box techniques and all the solvents were purified by distillation method in presence of proper drying agents. CDCl_3 was degassed through three freeze-pump-thaw cycles. The starting

materials $[\text{Cp}^*\text{VCl}_2]_3$,²⁷ $[\text{Cp}^*\text{NbCl}_4]$,²⁸ $[\text{Cp}^*\text{TaCl}_4]$,²⁹ $[\text{S}_2\text{C}\cdot\text{PPh}_3]$ ³⁰ and $[(\text{CH}_2\text{S}_2)_4\text{B}]\text{Na}_5$ ^{7,8} were synthesized following the corresponding literature. Thin-layer chromatography was performed using 250 mm aluminium supported silica gel TLC plates. Chemical shifts are referenced to residual solvent signals ($^1\text{H}/^{13}\text{C}\{^1\text{H}\}$; CDCl_3 ; $\delta = 7.26/77.16$ ppm). The 6545 Qtof LC/MS instrument was used for recording mass spectra of all compounds. JEOL Model JES FA200 instrument was used for the measurement of the electron paramagnetic resonance spectrum. UV-vis spectra were recorded on a JASCO V-650 spectrometer.

4.2 Synthesis of compound **1**

A freshly prepared solution of $[(\text{CH}_2\text{S}_2)_4\text{B}]\text{Na}_5$ (0.013 mmol in 10 mL tetrahydrofuran, 0.0013 mol/L) was added dropwise in the toluene (10 mL) solution of $[\text{Cp}^*\text{VCl}_2]_3$, (0.05g, 0.065 mmol), taken in a flame dried Schlenk tube, over 15 min at -78 °C. The reaction mixture was stirred vigorously and kept at 60 °C for 6 hours. Then the solvent was dried using vacuum and the solid deposit was extracted using the hexane/THF (90:10 v/v) solution mixture and ran through a G3 sintered frit partially filled with cotton. Then the volatiles were removed under vacuum and the chromatographic workup was carried out on silica gel TLC plates using the solid residue. The hexane/toluene (80:20 v/v) solution mixture was used as eluent and that allowed us to isolate yellow **1** (0.003 g, 11%) and **2**⁸ (0.007 g, 32%).

1: MS (ESI⁺) calcd for $\text{C}_{22}\text{H}_{33}\text{V}_2\text{S}_5^+$ $[\text{M}+\text{H}]^+$ m/z 559.0064, found 559.0039; UV-Vis $[\text{CH}_2\text{Cl}_2, \lambda, \text{nm}]$: 341, 463, 543. Well-grounded solid powder of complex **1** (~7 mg) was loaded into a sample holder under argon atmosphere and the X-band EPR spectrum was recorded at 77 K using the following parameters. Microwave frequency = 9136.87 MHz,

microwave power = 0.99800 mW, modulation frequency = 100.00 kHz, modulation amplitude CH1= 100.0, CH2 = 2.0, field centre = 400 mT, time constant CH1 = 0.1 s, CH2 = 0.03 s and sweep time = 2.0 min.

4.3 Synthesis of compound 3

A freshly prepared solution of $[(\text{CH}_2\text{S}_2)_4\text{B}]\text{Na}_5$ (0.027 mmol in 10 mL tetrahydrofuran, 0.0027 mol/L) was added dropwise in the toluene (10 mL) solution of $[\text{Cp}^*\text{NbCl}_4]$, (0.05g, 0.136 mmol), taken in a flame dried Schlenk tube, over 15 min at -78 °C. The reaction mixture was stirred vigorously and kept at 60 °C for 6 hours. Then the solvent was dried using vacuum and the solid deposit was extracted using the hexane/ CH_2Cl_2 (60:40 v/v) solution mixture and ran through a G3 sintered frit partially filled with cotton. Then the volatiles were removed under vacuum and the chromatographic workup was carried out on silica gel TLC plates using the solid residue. The hexane/ CH_2Cl_2 (60:40 v/v) solution mixture was used as eluent and that allowed us to isolate green **3** (0.005 g, 16%), and $[(\text{Cp}^*\text{Nb})_2(\mu, \eta^2: \eta^2\text{-SH}_3\text{B})(\mu\text{-S})(\mu\text{-H}_2\text{CS}_2\text{-}\kappa^2\text{S, S}')]^8$ (0.005 g, 11%).

3: MS (ESI⁺) calcd for $\text{C}_{21}\text{H}_{31}\text{Nb}_2\text{S}_5^+$ $[\text{M}+\text{H}]^+$ m/z 628.9157, found 628.9130; ^1H NMR (CDCl_3 , 500 MHz, 22 °C): δ = 2.17 ppm (s, 30H; $2 \times \text{Cp}^*$); $^{13}\text{C}\{^1\text{H}\}$ NMR (CDCl_3 , 125 MHz, 22 °C): δ = 12.8 ppm (s, C_5Me_5); UV-Vis [CH_2Cl_2 , λ , nm]: 347, 458, 533.

4.4 Synthesis of compounds 4 and 5

A freshly prepared solution of $[(\text{CH}_2\text{S}_2)_4\text{B}]\text{Na}_5$ (0.022 mmol in 10 mL tetrahydrofuran, 0.0022 mol/L) was added dropwise in the toluene (10 mL) solution of $[\text{Cp}^*\text{TaCl}_4]$, (0.05g, 0.110 mmol), taken in a flame dried Schlenk tube, over 15 min at -78 °C. The reaction mixture was stirred vigorously and kept at 60 °C for 6 hours. Then the

solvent was dried using vacuum and the solid deposit was extracted using the hexane/CH₂Cl₂ (40:60 v/v) solution mixture and ran through a G3 sintered frit partially filled with cotton. Then the volatiles were removed under vacuum and the chromatographic workup was carried out on silica gel TLC plates using the solid residue. The hexane/CH₂Cl₂ (40:60 v/v) solution mixture was used as eluent and that allowed us to isolate purple **4** (0.009 g, 28%) and orange **5** (0.005 g, 15%) along with [(Cp*Ta)₂(μ-S){μ-(BH₂S)(CH₂S)₂(BS₃)-κ²B:κ²S:κ⁴S',S'',S''',S''''}]⁸ (0.012 g, 24%).

4: MS (ESI+) calcd for C₂₃H₃₇Ta₂S₇⁺ [M+H]⁺ *m/z* 898.9900, found 898.9876; ¹H NMR (CDCl₃, 500 MHz, 22 °C): δ = 9.46 (s, 1H, Ta-*H*-Ta), 7.47 (s, 1H, CHS₃), 6.45 (d, ²J_{H-H} = 10.2 Hz, 1H, CH₂S₂), 4.28 (d, ²J_{H-H} = 10.7 Hz, 1H, CH₂S₂), 3.24 (d, ²J_{H-H} = 7.7 Hz, 1H, CH₂S₂), 2.90 (d, ²J_{H-H} = 10.7 Hz, 1H, CH₂S₂), 2.32, 2.26 ppm (s, 30H, 2×Cp*); ¹³C{¹H} NMR (CDCl₃, 125 MHz, 22 °C): δ = 120.5, 120.0 (s, C₅Me₅), 55.7 (s, CHS₃), 49.9, 47.8 (s, CH₂S₂), 12.7, 12.6 ppm (s, C₅Me₅); UV-Vis [CH₂Cl₂, λ, nm]: 371, 511.

5: MS (ESI+) calcd for C₂₂H₃₅Ta₂S₅⁺ [M-Cl]⁺ *m/z* 821.0302, found 821.0310; ¹H NMR (CDCl₃, 400 MHz, 22 °C): δ = 10.77 (s, 1H, Ta-*H*-Ta), 7.43 (d, ²J_{H-H} = 11.1 Hz, 1H, CH₂S₂), 5.95 (d, ²J_{H-H} = 10.6 Hz, 1H, CH₂S₂), 4.55 (d, ²J_{H-H} = 10.6 Hz, 1H, CH₂S₂), 4.15 (d, ²J_{H-H} = 10.6 Hz, 1H, CH₂S₂), 2.31, 2.24 ppm (s, 30H, 2×Cp*); ¹³C{¹H} NMR (CDCl₃, 100 MHz, 22 °C): δ = 120.9, 119.4 (s, C₅Me₅), 56.7 (s, CH₂S₂), 43.3 (s, CH₂S₂), 12.6, 12.3 ppm (s, C₅Me₅); UV-Vis [CH₂Cl₂, λ, nm]: 369, 432, 504.

4.5 Synthesis of compound **6**

A 2.0 M LiBH₄·THF solution (0.7 mL) was added dropwise in the toluene (10 mL) solution of [Cp*TaCl₄], (0.100 g, 0.22 mmol), taken in a flame dried Schlenk tube, over 15 min at -78 °C. The mixture was allowed to stir for 1 hour, then the freshly prepared solution of excess S₂C·PPh₃ (0.075 g of PPh₃ dissolved in 6 mL of CS₂) was added over 5 min and the reaction mixture was stirred vigorously and kept at 60 °C for 6 hours. The reaction mixture color changed from yellow to brown. Then, the solvent was dried using vacuum and the solid deposit was extracted using the hexane/CH₂Cl₂ (40:60 v/v) solution mixture and ran through a G3 sintered frit partially filled with cotton. Then the volatiles were removed under vacuum and the chromatographic workup was carried out on silica gel TLC plates using the solid residue. The hexane/CH₂Cl₂ (40:60 v/v) solution mixture was used as eluent and that allowed us to isolate orange **6** (0.014 g, 15%) and [(Cp*Ta)₂(μ-S₂CH₂-κ²S:κ²S')₂(μ-H)(μ,η²:η²-B₂H₅)]⁹ **7** (0.0125 g, 14%) and [(Cp*Ta)₂(B₂H₆)₂]²² (0.025 g, 33%).

6: MS (ESI+) calcd for C₂₃H₃₇Ta₂S₇Na⁺ [M+Na]⁺ *m/z* 874.9842, found 874.9845; ¹H

NMR (CDCl₃, 500 MHz, 22 °C): δ = 11.34 (s, 1H, Ta-*H*-Ta), 7.37 (s, 1H, CHS₃), 7.34 (dd, ²J_{H-H} = 10.4 Hz, 1H, CH₂S₂), 6.02 (d, ²J_{H-H} = 10.4 Hz, 1H, CH₂S₂), 2.23 ppm (s, 30H, 2×Cp*); ¹³C{¹H} NMR (CDCl₃, 125 MHz, 22 °C): δ = 119.6 (s, C₅Me₅), 68.1 (s, CHS₃),

25.8 (s, CH₂S₂), 12.4 ppm (s, C₅Me₅); UV-Vis [CH₂Cl₂, λ, nm]: 370, 473.

4.6 X-ray structure determination

The crystal data of **1** and **6** were collected and integrated using Bruker APEX3 diffractometer with graphite monochromated Mo-Kα (λ = 0.71073 Å) radiation at 296(2) K. The

crystal data of **3** and **4** were collected and integrated using D8 VENTURE Bruker AXS diffractometer with graphite monochromated Mo-K α ($\lambda = 0.71073$ Å) radiation at 150(2) K. The crystal data of **5** was collected and integrated using Bruker APEX2 diffractometer with graphite monochromated Mo-K α ($\lambda = 0.71073$ Å) radiation at 296(2) K. The molecular structure of **1** was solved by heavy atom methods using SHELXT-2014/5 and refined using SHELXL-2018/3.³¹ The structures of **3** and **4** were solved by heavy atom methods using SHELXT-2014/4 and refined using SHELXL-2017/1.³¹ The structures of **5** and **6** was solved by heavy atom methods using SHELXS-97 and refined using SHELXL-2018/3.³¹ Olex² software was used to draw all the molecular structures.³² The non-hydrogen atoms were refined with anisotropic displacement parameters. All hydrogens could not be located in the difference Fourier map for compound **4**.

(Table 3 near here)

4.7 Computational details

Geometry optimizations and electronic structure calculations were carried out on the Gaussian 09 program³³ package using the BP86 functional³⁴ and the triple- ζ quality basis set def2-TZVP³⁵. In compound **1** both the vanadium centers are in (+III) oxidation state i.e. d^2 electronic configuration. So, there are possibilities of both, low spin diamagnetic singlet state (multiplicity = 1) configuration and high spin triplet state (multiplicity = 3) configuration. And calculation shows that the triplet spin state ($E = -4737.74600201$ a.u.) is more stable than diamagnetic singlet spin state ($E = -4737.73137247$ a.u.) by 0.01462954 a.u. In case of compound **3**, **4**, **5** and **6** both the metal centers are in (+V) oxidation state i.e. d^0 electronic configuration. So, there is the only possibility of the low spin diamagnetic singlet state configuration. Therefore, for the optimization and other theoretical analyses of compound **1**, multiplicity = 3 and for other molecules, multiplicity = 1 has been considered. Vibrational

analyses were carried out for all structures, and the absence of any imaginary frequency confirmed that all structures represent minima on the potential energy hypersurface. The gauge including atomic orbital (GIAO)³⁶ method was employed to calculate the NMR chemical shifts of the BP86/def2-TZVP optimized geometries using the hybrid Becke–Lee–Yang–Parr (B3LYP)³⁷ functional and aforementioned basis set. For computing ¹H NMR chemical shift, TMS(SiMe₄) has been taken as the internal standard (shielding constant 31.92 ppm). Natural bonding analyses were performed with the NBO partitioning scheme, as implemented in the Gaussian 09 suite of programs.³⁸ Wiberg bond indexes (WBI) were obtained on NBO analysis.³⁹ All the optimized structures and orbital plots were generated by using visualization programs, such as Gaussview⁴⁰ and Chemcraft⁴¹. In order to understand the nature of bonding of the synthesized molecules in greater detail, the topological properties of the resultant electron density, ρ , obtained from the wave functions of all of the optimized structures were analyzed with the quantum theory of atoms in molecules (QTAIM).⁴² QTAIM analysis was carried out utilizing the Multiwfn, V.3.6, package⁴³ whereas the wave functions were generated with Gaussian 09 at the same level of theory as that used for geometry.

Declaration of Competing Interest

The authors declare no competing financial interest.

Acknowledgements

The support from Indo-French Center for the Promotion of Advanced Research (IFCPAR-CEFIPRA), Project No. 5905-1 is gratefully acknowledged. S.B. thanks IIT Madras and A.D.

thanks CSIR for research fellowships. The computational facility, IIT Madras, is thankfully acknowledged. The authors thank Prof. Chandan Mukherjee of IIT Guwahati, for his help with EPR simulation.

Appendix A. Supplementary data

Supplementary data related to this article can be found at <http://dx.doi.org>

References

- [1] (a) R. L. Robson, R. R. Eady, T. H. Richardson, R. W. Miller, M. Hawkins, J. R. Postgate, *Nature* 322 (1986) 388–390; (b) B. J. Hales, E. E. Case, J. E. Morningstar, M. F. Dzeda, L. A. Mauterer, *Biochemistry* 25 (1986) 7251–7255; (c) K. Kustin, I. G. Macara, *Inorg. Chem.* 2 (1982) 1–22.
- [2] (a) J. R. Dilworth, J. Hu, *Adv. Inorg. Chem.* 40 (1993) 411–459; (b) B. Krebs, G. Henkel, *Angew. Chem., Int. Ed. Engl.* 30 (1991) 769–788; (c) P. J. Blower, J. R. Dilworth, *Coord. Chem. Rev.* 76 (1987), 121–185; (d) I. G. Dance, *Polyhedron* 5 (1986) 1037–1104; (e) R. D. Adams, T. Barnard, A. Rawlett, J. M. Tour, *Eur. J. Inorg. Chem.* (1998), 1998 429–431.
- [3] (a) F. E. Massoth, *Adv. Catal.* 27 (1979), 265–310; (b) W. L. Orr, *Oil Sand, Oil Shale Chemistry*, Verlag Chemie, Weinheim, (1978), p. 223; (c) T. D. Cyr, J. D. Payzant, D. S. Montgomery, O. P. Strausz, *Org. Geochem.* 9 (1986) 139–143; (d) M. Nishioka, *Energy Fuels* 2 (1988) 214–219.
- [4] (a) M. Bochmann, I. Hawkins, L. M. Wilson, *J. Chem. Soc., Chem. Commun.* (1988) 344–345; (b) B. Hasenknopf, *Frontiers in Bioscience* 10 (2005) 275–287.
- [5] (a) J. R. Dorfman, R. H. Holm, *Inorg. Chem.* 22 (1983) 3179–3181; (b) D. Szymies, B. Krebs, G. Henkel, *Angew. Chem. Int. Ed. Engl.* 22 (1983) 885–886.
- [6] (a) K. Saha, S. Kar, U. Kaur, T. Roisnel, S. Ghosh, *Organometallics* 39 (2020) 4362–4371; (b) S. Kar, S. Bairagi, K. Saha, B. Raghavendra, S. Ghosh, *Dalton Trans.* 48 (2019) 4203–4210; (c) K. Saha, U. Kaur, R. Borthakur, S. Ghosh, *Inorganics* 7 (2019) 21; (d) K. Saha, U. Kaur, S. Kar, B. Mondal, B. Joseph, P. K. S. Antharjanam, S. Ghosh, *Inorg. Chem.* 58

- (2019) 2346–2353; (e) S. Kar, K. Saha, S. Saha, K. Bakthabachalam, V. Dorcet, S. Ghosh, *Inorg. Chem.* 57 (2018) 10896–10905.
- [7] (a) B. Joseph, K. Saha, R. Prakash, C. Nandi, T. Roisnel, S. Ghosh, *Inorg. Chim. Acta.* 483 (2018) 106–110; (b) K. Saha, S. Kar, S. Ghosh, *J. Indian Chem. Soc.* 95 (2018), 729; (c) R. Ramalakshmi, K. Saha, A. Paul, S. Ghosh, *J. Chem. Sci.* 128 (2016) 1025–1032.
- [8] K. Saha, U. Kaur, B. Raghavendra, S. Ghosh, *Inorg. Chem.* 59 (2020) 12494–12503.
- [9] K. Saha, S. Ghorai, S. Kar, S. Saha, R. Halder, B. Raghavendra, E. D. Jemmis, S. Ghosh, *Angew. Chem. Int. Ed.* 58 (2019) 1–7.
- [10] W. Diamantikos, H. Heinzelmann, E. Rath, H. Binder, *Z. Anorg. Allg. Chem.* 517 (1984) 111–117.
- [11] (a) S. K. Bose, K. Geetharani, V. Ramkumar, S. M. Mobin, S. Ghosh, *Chem. Eur. J.* 15 (2009) 13483–13490; (b) H. Brunner, G. Gehart, W. Meier, J. Wachter, B. Wrackmeyer, B. Nuber, M. L. Ziegler, *J. Organomet. Chem.* 436 (1992) 313–324.
- [12] (a) M. G. Chowdhury, S. K. Barik, K. Saha, K. Bakthavachalam, A. Banerjee, V. Ramkumar, S. Ghosh, *Inorg. Chem.* 57 (2018) 985–994; (b) B. Mondal, R. Bag, K. Bakthavachalam, B. Varghese, S. Ghosh, *Eur. J. Inorg. Chem.* (2017) 5434–5441; (c) R. Ramalakshmi, T. Roisnel, V. Dorcet, J.-F. Halet, S. Ghosh, *J. Organomet. Chem.* 849–850 (2017) 256–260.
- [13] O. A. Rajan, M. McKenna, J. Noordik, R. C. Haltiwanger, M. R. DuBois, *Organometallics* 3 (1984) 831–840.
- [14] M. McKenna, L. L. Wright, D. J. Miller, L. Tanner, R. C. Haltiwanger, M. R. Dubois, *J. Am. Chem. Soc.* 105 (1983) 5329–5331.
- [15] (a) J. Krzysteka, A. Ozarowskia, J. Telsorb, D. C. Cransc, *Coord. Chem. Rev.* 301–302 (2015) 123–133; (b) B. E. Petel, E. M. Matson, *Inorg. Chem.* (2020) (doi.org/10.1021/acs.inorgchem.0c02052).
- [16] (a) K. R. Kittilstved, A. Hauser, *Coord. Chem. Rev.* 254 (2010) 2663–2676; (b) D. C. Horton, D. VanDerveer, J. Krzystek, J. Telsor, T. Pittman, D. C. Crans, A. Holder, *Inorg. Chim. Acta.* 420 (2014) 112–119.

- [17] (a) C. D. Abernethy, F. Bottomley, A. Decken, *Organometallics* 16 (1997) 1865–1869; (b) B. L. Tran, J. Krzystek, A. Ozarowski, C.-H. Cheng, M. Pink, J. A. Kart, J. Telsler, K. Meyer, D. J. Mindiola, *Eur. J. Inorg. Chem.* 2013, 3916–3929.
- [18] M. Gomez, C. Hernandez-Prieto, A. Martin, M. Mena, C. Santamaria, *J. Organomet. Chem.* 897 (2019) 148–154.
- [19] (a) C. E. Rao, S. K. Barik, K. Yuvaraj, K. Bakthavachalam, T. Roisnel, V. Dorcet, J.-F. Halet, S. Ghosh, *Eur. J. Inorg. Chem.* (2016), 4913–4920; (b) A. Galindo, C. Mealli, J. Cayas, D. Miguel, V. Riera, J. A. Perez-Martinez, C. Bois, Y. Jeannin, *Organometallics* 15 (1996) 2735–2744.
- [20] B. Li, X. Tan, S. Xu, H. Song, B. Wang, *J. Organomet. Chem.* 693 (2008), 667–674.
- [21] (a) C. Bianchini, P. Innocenti, A. Meli, *J. Chem. Soc., Dalton Trans.* 8 (1983) 1777–1781; (b) R. Usón, J. Forniés, M. A. Usón, *Synthesis and Reactivity in Inorganic and Metal-Organic Chemistry* 14 (1984) 355–367; (c) M. T. Whited, L. Qiu, A. J. Kosanovich, D. E. Janzen, *Inorg. Chem.* 54 (2015) 3670–3679; (d) J. Vicente, M. T. Chicote, P. Gonzalez-Herreroa, P. G. Jones, *J. Chem. Soc., Chem. Commun.* (1995), 745–746.
- [22] (a) S. K. Bose, K. Geetharani, B. Varghese, S. M. Mobin, S. Ghosh, *Chem. Eur. J.* 14 (2008) 9058–9064; (b) A. J. Scioly, M. L. Luetkens Jr., R. B. Wilson Jr., J. C. Huffman, A. P. Sattleberger, *Polyhedron* 6 (1987) 741–757; (c) R. Prakash, K. Bakthavachalam, B. Varghese, S. Ghosh, *J. Organomet. Chem.* 846 (2017) 372–378.
- [23] D. Sellmann, M. Wille, F. Knoch, *Inorg. Chem.* 32 (1993) 2534–2543.
- [24] R. H. D. Lyngdoh, H. F. Schafer III, R. B. King. *Chem. Rev.* 118 (2018) 11626–11706.
- [25] P. Govindaswamy, Y. A. Mozharivskyj, M. R. Kollipara, *Polyhedron* 24 (2005) 1710–1716.
- [26] A. Haridas, S. Kar, B. Raghavendra, T. Roisnel, V. Dorcet, S. Ghosh, *Organometallics* 39 (2020) 58–65.
- [27] C. D. Abernethy, F. Bottomley, A. Decken, *Organometallics* 16 (1997) 1865–1869.
- [28] T. Okamoto, H. Yasuda, A. Nakamura, Y. Kai, N. Kanehisa, N. Kasai, *J. Am. Chem. Soc.* 110 (1988) 5008–5017.

- [29] Z. J. Tonzetich, R. Eisenberg, *Inorg. Chim. Acta.* 345 (2003) 340-344.
- [30] (a) S. M. Boniface, G. R. J. Clark, *Organomet. Chem.* 188 (1980) 263–275; (b) I. S. Butler, in *Inorganic Reactions and Methods, The Formation of Bonds to Elements of Group IVB (C, Si, Ge, Sn, Pb) (Part 4)*, Vol 12B, (Eds.: J. J. Zuckerman, A. P. Hagen) (1991) Wiley-VCH, pp. 206–209.
- [31] G. M. Sheldrick, *Acta Crystallogr. Sect. C* 71 (2015) 3–8.
- [32] O. V. Dolomanov, L. J. Bourhis, R. J. Gildea, J. A. K. Howard, H. Puschmann, *J. Appl. Cryst.* 42 (2009) 339–341.
- [33] Gaussian 09, Revision C.01, M. J. Frisch, G. W. Trucks, H. B. Schlegel, G. E. Scuseria, M. A. Robb, J. R. Cheeseman, G. Scalmani, V. Barone, B. Mennucci, G. A. Petersson, H. Nakatsuji, M. Caricato, X. Li, H. P. Hratchian, A. F. Izmaylov, J. Bloino, G. Zheng, J. L. Sonnenberg, M. Hada, M. Ehara, K. Toyota, R. Fukuda, J. Hasegawa, M. Ishida, T. Nakajima, Y. Honda, O. Kitao, H. Nakai, T. Vreven, J. A. Montgomery, Jr. J. E. Peralta, F. Ogliaro, M. Bearpark, J. J. Heyd, E. Brothers, K. N. Kudin, V. N. Staroverov, T. Keith, R. Kobayashi, J. Normand, K. Raghavachari, A. Rendell, J. C. Burant, S. S. Iyengar, J. Tomasi, M. Cossi, N. Rega, J. M. , M. Klene, J. E. Knox, J. B. Cross, V. Bakken, C. Adamo, J. Jaramillo, R. Gomperts, R. E. Stratmann, O. Yazyev, A. J. Austin, R. Cammi, C. Pomelli, J. W. Ochterski, R. L. Martin, K. Morokuma, V. G. Zakrzewski, G. A. Voth, P. Salvador, J. J. Dannenberg, S. Dapprich, A. D. Daniels, O. Farkas, J. B. Foresman, J. V. Ortiz, J. Cioslowski, D. J. Fox, Gaussian Inc., Wallingford CT (2010).
- [34] (a) H. L. Schmider, A. D. Becke, *J. Chem. Phys.* 108 (1998) 9624–9631; (b) J. P. Perdew, *Phys. Rev. B: Condens. Matter Mater. Phys.* 33 (1986) 8822–8824.
- [35] (a) F. Weigend, R. Ahlrichs, *Phys. Chem. Chem. Phys.* 7 (2005) 3297–3305.
- [36] (a) F. J. London, *J. Phys. Radium* 8 (1937) 397–409; (b) R. Ditchfield, *Mol. Phys.* 27 (1974) 789–807; (c) K. Wolinski, J. F. Hinton, P. Pulay, *J. Am. Chem. Soc.* 112 (1990) 8251–8260.
- [37] (a) A. D. Becke, *J. Chem. Phys.* 98 (1993), 5648–5652; (b) A. D. Becke, *Phys. Rev. A.* 38 (1988) 3098–3100; (c) C. Lee, W. Yang, R. G. Parr, *Phys. Rev. B.* 37 (1988) 785–789.
- [38] (a) E. D. Glendening, A. E. Reed, J. E. Carpenter, F. Weinhold, NBO Program 3.1, W. T. Madison (1988); (b) A. E. Reed, L. A. Curtiss, F. Weinhold, *Chem. Rev.* 88 (1988) 899–926; (c) F. Weinhold, C. R. Landis, *Valency and Bonding: A Natural Bond Orbital Donor-Acceptor Perspective*, Cambridge University Press, Cambridge (2005).

- [39] K. Wiberg, *Tetrahedron* 24 (1968) 1083–1096.
- [40] GaussView, Version 3.09, II. R. T. Dennington Keith, J. Millam, K. Eppinnett, W. L. Hovell, R. Gilliland, Inc, Semichem, Shawnee Mission KS (2003).
- [41] G. A. Zhurko, <http://www.chemcraftprog.com>.
- [42] (a) R. F. W. Bader, *Atoms in Molecules: a Quantum Theory*; Oxford University Press: Oxford, U.K. (1990); (b) R. F. W. Bader, *J. Phys. Chem. A.* 102 (1998) 7314–7323; (c) R. F. W. Bader, *Chem. Rev.* 91 (1991) 893–928.
- [43] T. Lu, F. Chen, *J. Comput. Chem.* 33 (2012) 580–592.

Journal Pre-proof

Scheme 1 Syntheses of vanadium thiolate complexes.

Scheme 2. Syntheses of thiolate complexes of niobium and tantalum.

Scheme 3. Synthesis of thiolate complex of tantalum **6**.

Fig. 1. Molecular structure and labelling diagram of **1**. Selected bond lengths (Å) and angles (°) are: V1-S1 2.4550(10), V1-S2 2.4484(10), V1-S4 2.4256(10), V1-S5 2.4247(10), V1-V2 2.5548(7), V2-S1 2.4504(10), V2-S2 2.4507(10), V2-S4 2.4318(10), V2-S5 2.4228(10), C21-S1 1.747(4), C21-S2 1.751(4), C21-S3 1.622(4), C22-S4 1.835(4), C22-S5 1.833(4); V1-S1-V2 62.77(3), V1-S2-V2 62.87(3), V1-S4-V2 63.47(3), S1-C21-S2 106.24(18), S4-C22-S5 99.43(19).

Fig. 2. (a) α -SOMO-2, (b) α -SOMO-9 and (c) α -SOMO-13 of **1**. Contour values are $\pm 0.04 (e/\text{bohr}^3)^{1/2}$. (d) and (e) Contour line diagram of the Laplacian of the electron density ($\nabla^2\rho(r)$) in V1-S1-V2 plane and the perpendicular plane with respect to V-V bond. The dashed black line displays the area of charge depletion ($\nabla^2\rho(r) > 0$) and the solid red line shows the area of charge concentration ($\nabla^2\rho(r) < 0$). Deep Brown line indicates the bond path whereas blue dot depicts the bond critical point (BCP).

Fig. 3. X-band EPR spectrum of the solid sample of complex **1** recorded at 77 K with microwave frequency of 9.136 GHz.

Fig. 4. Molecular orbitals showing α and β subspaces for the antiferromagnetically coupled vanadium centres in **1**. Contour values are $\pm 0.05 (e/\text{bohr}^3)^{1/2}$.

Fig. 5. Molecular structure and labelling diagram of and **3**. The protons of Cp* rings are not shown for clarity. Selected bond lengths (Å) and angles (°) are: Nb1-S1 2.4557(7), Nb1-S2 2.4412(7), Nb1-Nb2 2.9705(3), C31-S1 1.756(3), C31-S2 1.746(3), C31-S5 1.776(3), Nb2-S5 2.3977(7), Nb1-C31 2.259(2); S1-C31-S2

112.26(14), S1-C31-S5 123.46(16), S2-C31-S5 123.92(15), C31-S5-Nb2 86.26(8), S5-C31-Nb1 125.15(13).

Fig. 6. (a) HOMO-1, (b) HOMO-8 and (c) HOMO-25 of **3**. Contour values are ± 0.04 $(\text{e}/\text{bohr}^3)^{1/2}$. (d) and (e) Contour line diagram of Laplacian of the electron density $\nabla^2\rho(r)$ in Nb2-Nb1-C31 and S1-S2-S5 plane, respectively. The dashed black line displays the area of charge depletion ($\nabla^2\rho(r) > 0$) and the solid red line shows the area of charge concentration ($\nabla^2\rho(r) < 0$). Deep Brown line indicates the bond path whereas blue dot depicts the bond critical point (BCP).

Fig. 7. Molecular structure and labelling diagram of **4** (left) and **5** (right). The bridging hydrogen atom and the protons of Cp* rings are not shown for clarity. Selected bond lengths (\AA) and angles ($^\circ$) are: **4**: Ta1-S1 2.4389(14), Ta1-S4 2.4470(13), Ta1-S6 2.5641(14), Ta2-S5 2.4419(14), Ta1-Ta2 3.1156(3), S1-C21 1.826(6), S4-C22 1.826(6), S6-C23 1.838(6), S7-C23 1.792(6), S7-C22 1.821(6); C21-S1-Ta1 106.7(2), Ta2-S3-Ta1 80.72(4), C22-S4-Ta1 113.1(2). **5**: Ta1-S3 2.411(4), Ta1-S1 2.392(6), Ta1-S4 2.600(2), Ta1-S5 2.544(16), Ta1-Ta2 3.1483(8), Ta2-C11 2.463(14), Ta2-S4 2.590(17), S1-C21 1.850(2), S4-C22 1.900(2); C21-S1-Ta1 108.7(7), Ta2-S3-Ta1 81.43(13), C22-S4-Ta1 93.00(9).

Fig. 8. Comparison of frontier molecular orbitals of **4**, **5** and **6**; respectively. Contour values are ± 0.04 $(\text{e}/\text{bohr}^3)^{1/2}$.

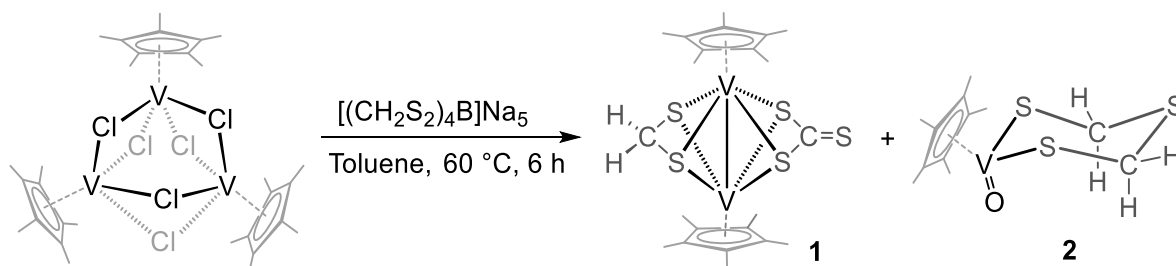
Fig. 9. Combined UV-vis spectra of **1**, **3**, **4**, **5** and **6** in CH_2Cl_2 .

Table 1. Examples of transition metal complexes with unique coordination modes of bridging $\{\mu\text{-CS}_3\}$ ligand.

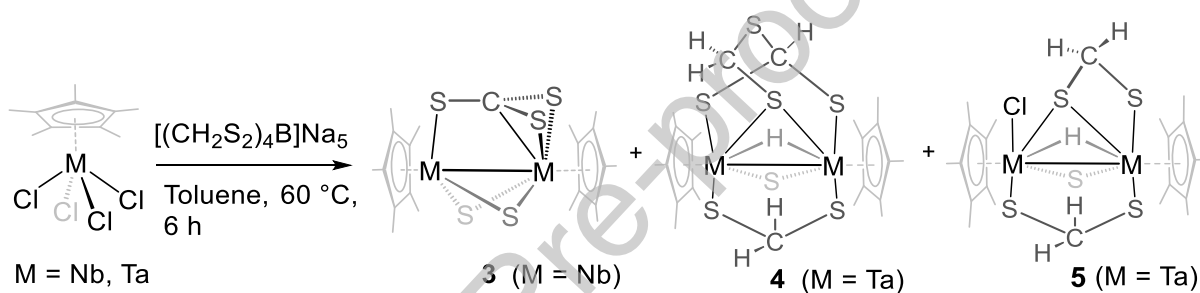
Table 2. Selected structural and spectroscopic parameters of binuclear metal thiolate complexes.

Table 3. Crystal data and structure refinement details for compounds **1**, **3**, **4** and **5**.

Scheme 1



Scheme 2



Scheme 3

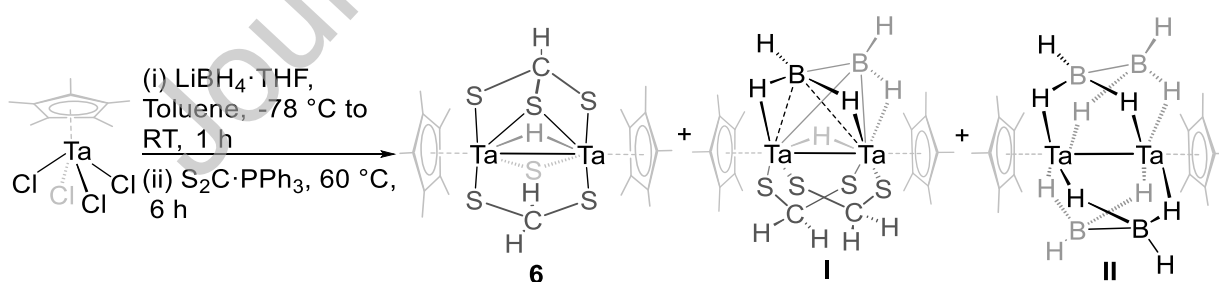


Fig. 1

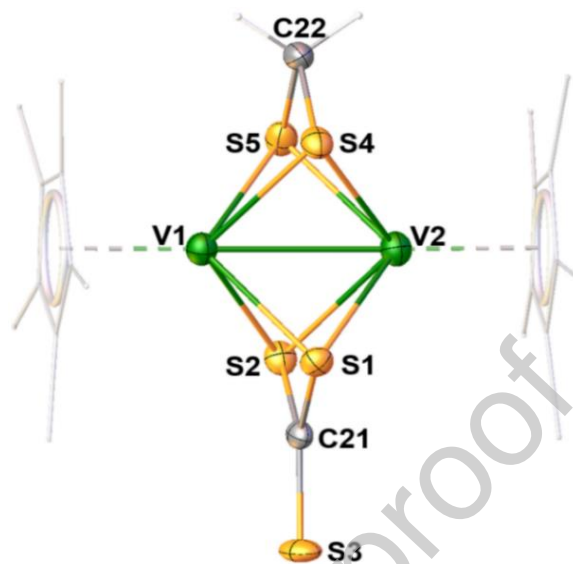


Fig. 2

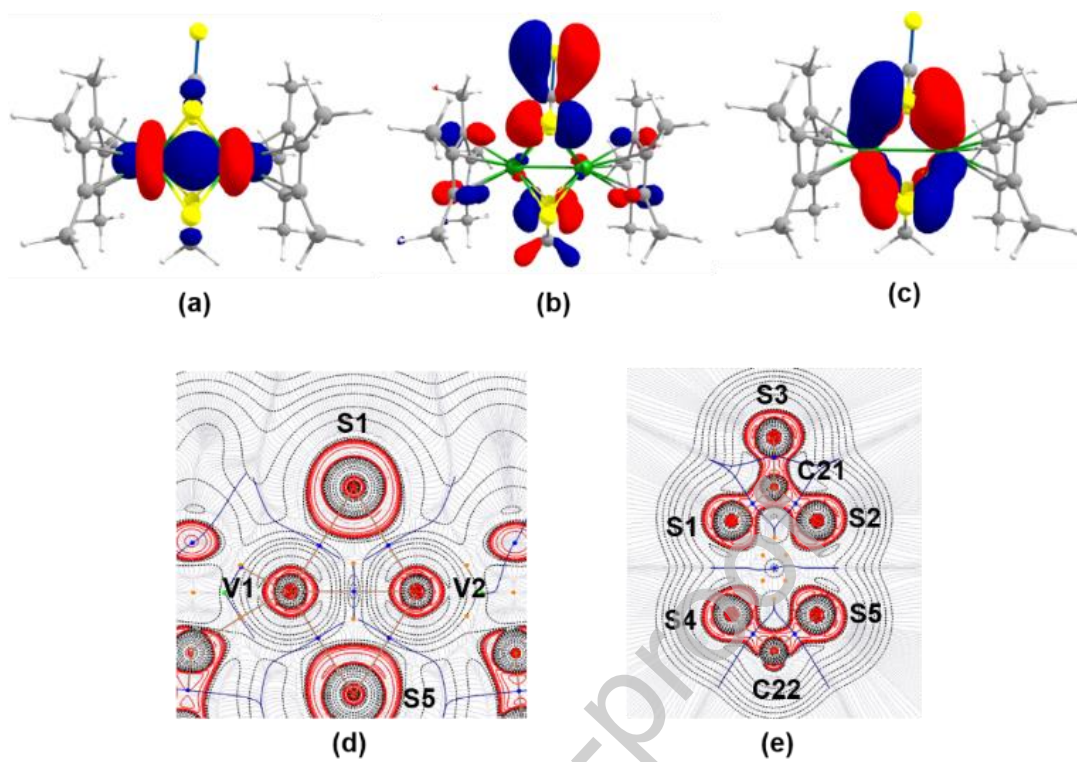


Fig. 3

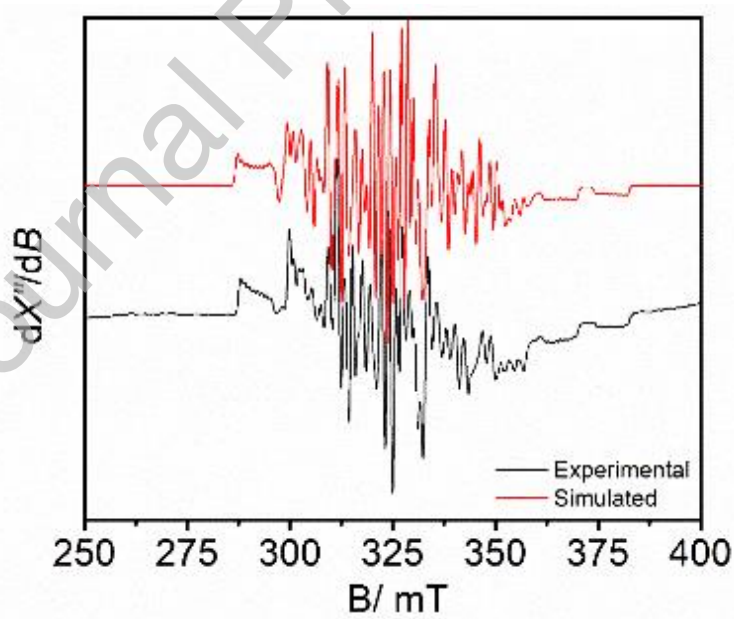


Fig. 4

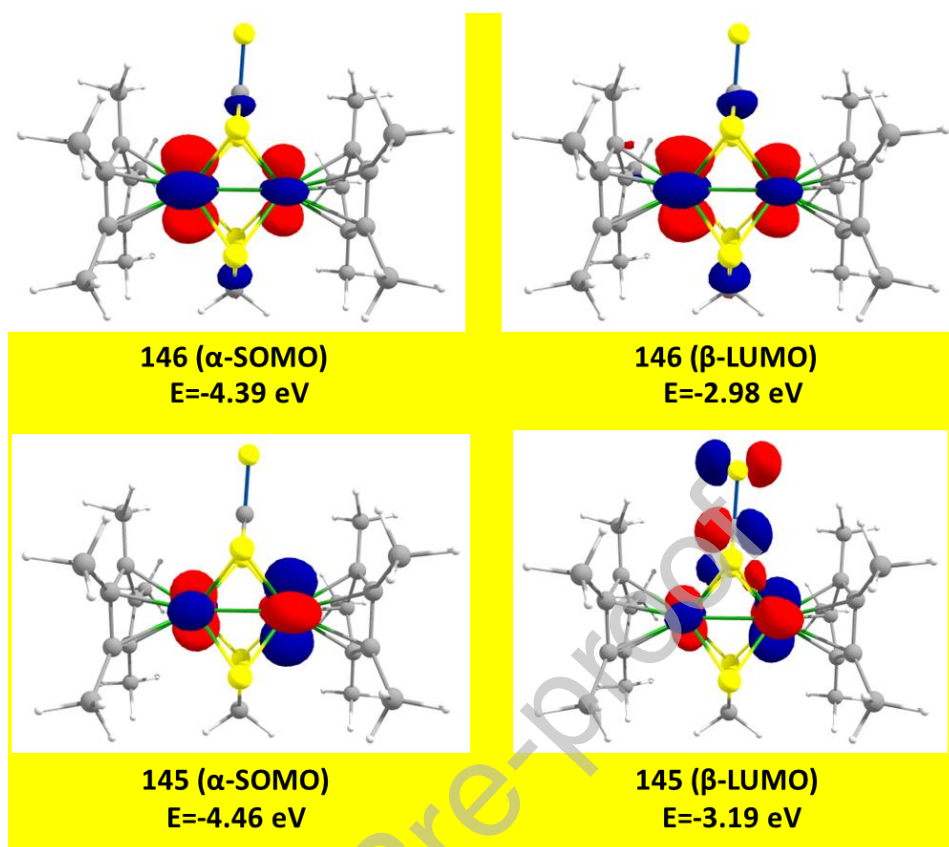


Fig. 5

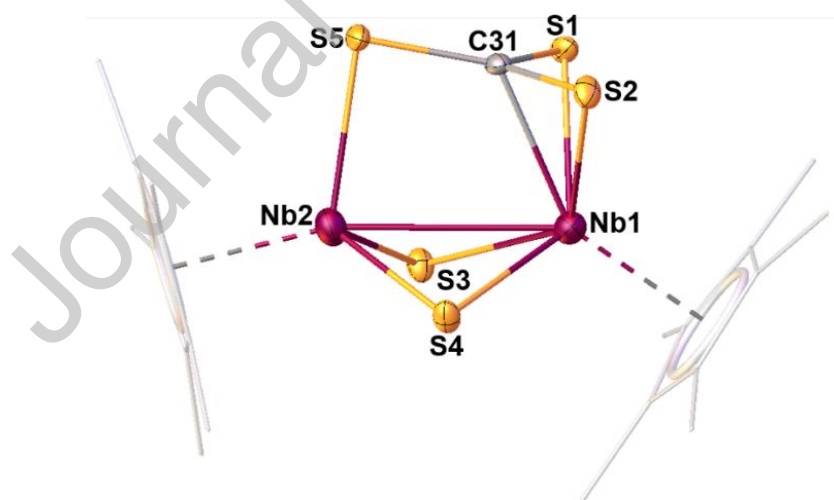


Fig. 6

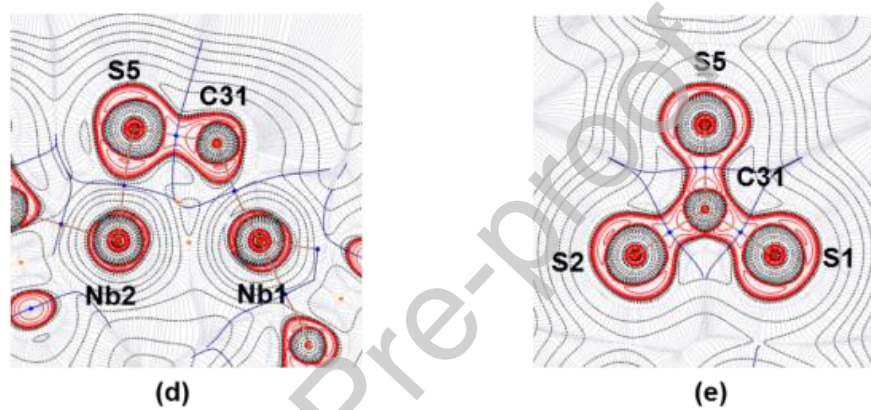
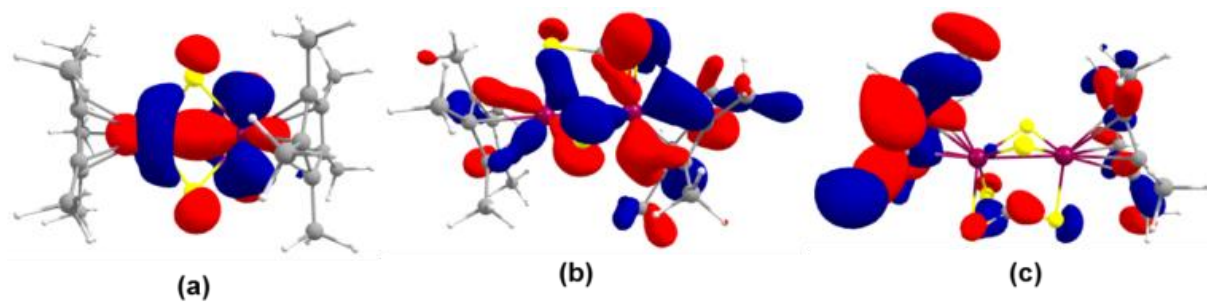


Fig. 7

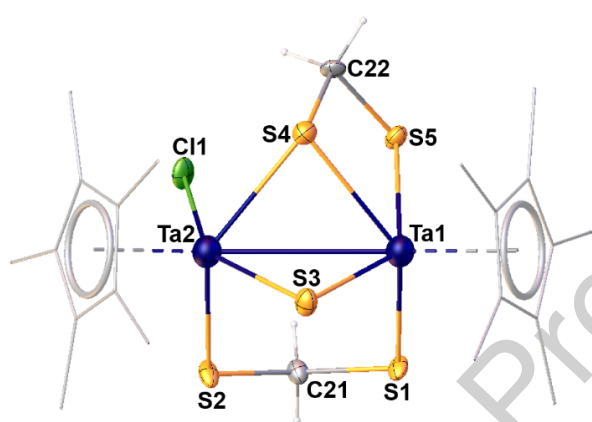
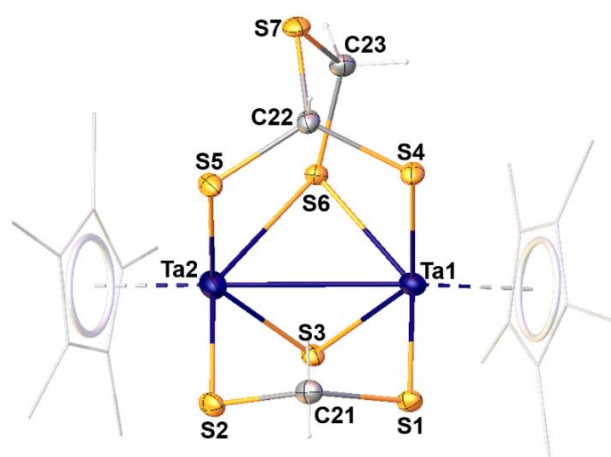


Fig. 8

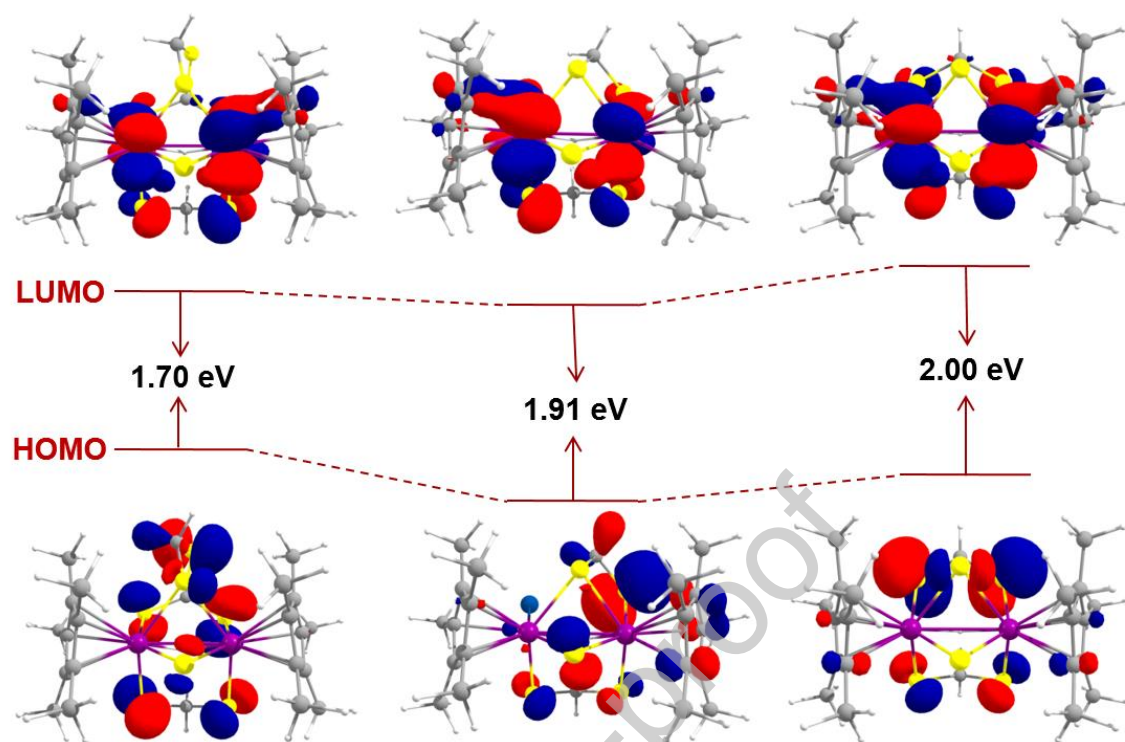


Fig. 9

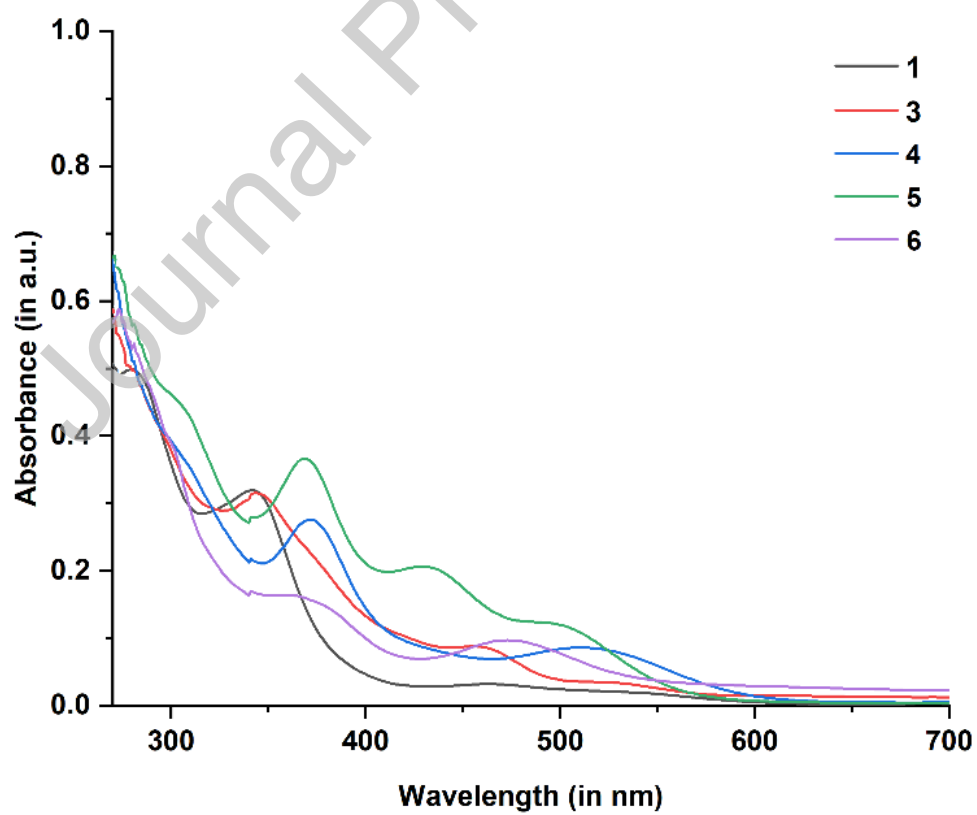
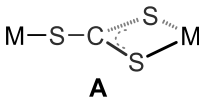
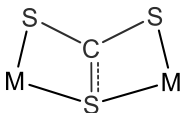
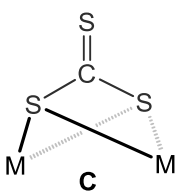
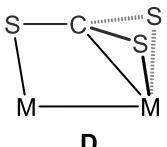
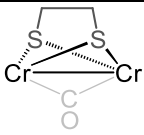
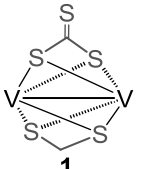
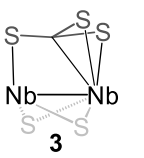
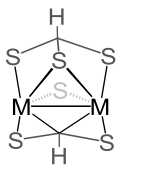
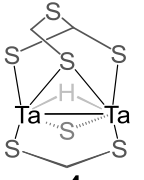
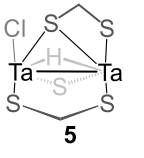
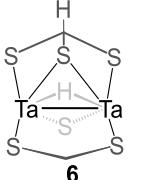
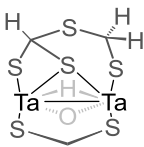


Table 1

Complex	Metal (M)	\angle S-C-S ($^{\circ}$) ^a	Ref.
 <p style="text-align: center;">A</p>	Mo, Ni ^b , Pd ^b , Re ^b	110.6	12c, 21a,b
 <p style="text-align: center;">B</p>	Mo	119.6	20
 <p style="text-align: center;">C</p>	Mo, Rh, Au, V (1)	121.8 (Mo), 119.9 (Rh), 120.0 (Au), 114.8 (V)	19a, 21c,d, This work
 <p style="text-align: center;">D</p>	Nb (3)	119.9	This work

^a = Average, ^b = structural data not available.

Table 2

Complex	Structural parameters			Spectroscopic data	Ref.
	d(M-M) (Å)	d _{avg} (M-S) (Å)	∠M-S-M (°)	δ _H (ppm, ² J _{H-H} (Hz)) ^a	
	2.698(3)	2.419	67.8	-	23
 1	2.5548(7)	2.439	62.77 63.47	-	this work
 3	2.9705(3)	2.417	75.81 76.36	-	this work
 M = Cp*Nb, Cp*Ta	3.173 (Nb) 3.171 (Ta)	2.441 (Nb) 2.457 (Ta)	77.90 (Nb) 88.04 (Nb) 77.99 (Ta) 82.61 (Ta)	6.93, 6.33 7.07, 5.55	8
 4	3.1155(3)	2.472	73.49 80.71	6.45 (10.2), 4.28 (10.7), 3.24 (7.7), 2.90 (10.7)	this work
 5	3.1483(8)	2.478	75.00 81.43	7.43 (11.1), 5.95 (10.6), 4.55 (10.6), 4.15 (10.6)	this work
 6	-	-	-	7.34 (10.4), 6.02 (10.4)	this work
	2.9882(5)	2.490	70.39	6.68 (13.7), 6.24 (10.7), 4.61 (13.7)	8

^a = for methylene or methine protons, avg = average, V = Cp*V, Nb = Cp*Nb and Ta = Cp*Ta

Table 3

Complex	1	3	4	5
CCDC no.	1945969	1945970	1945975	2071639
Empirical formula	C ₂₂ H ₃₂ V ₂ S ₅	C ₂₁ H ₃₀ Nb ₂ S ₅	C ₂₃ H ₃₅ Ta ₂ S ₇	C ₂₂ H ₃₅ Ta ₂ S ₅ Cl
Formula weight	558.65	628.57	897.83	857.15
Crystal system	Monoclinic	Triclinic	Monoclinic	Monoclinic
Space group	<i>P</i> 2 ₁ / <i>c</i>	<i>P</i> -1	<i>P</i> 2 ₁ / <i>c</i>	<i>P</i> 2 ₁ / <i>c</i>
<i>a</i> (Å)	10.4292(3)	9.1745(3)	16.8392(6)	11.9775(17)
<i>b</i> (Å)	14.6090(4)	15.1004(5)	13.6634(5)	29.366(3)
<i>c</i> (Å)	16.9179(4)	19.1683(7)	16.1271(6)	8.2341(9)
α (°)	90	103.318(2)	90	90
β (°)	103.869(2)	101.8920(10)	107.345(2)	109.978(2)
γ (°)	90	100.3930(10)	90	90
<i>V</i> (Å ³)	2502.47(12)	2455.20(15)	3541.8(2)	2722.0(6)
<i>Z</i>	4	4	4	4
ρ_{calcd} (g/cm ³)	1.483	1.700	1.684	2.092
μ (mm ⁻¹)	1.172	1.365	6.597	8.525
<i>F</i> (000)	1160	1272	1724	1640
<i>R</i> ₁	0.0397	0.0315	0.0332	0.0516
<i>wR</i> ₂	0.0720	0.0779	0.0695	0.1140
Independent reflections	3511	9334	6598	3537
2 θ ≤ (°)	50.00	54.966	54.966	50.00
Parameters	272	525	299	313

Journal Pre-proof